Towards Online Iris and Periocular Recognition under Relaxed Imaging Constraints

Chun-Wei Tan, Ajay Kumar

Abstract: *Online iris recognition using distantly acquired images under less imaging constrained environment requires the development of efficient iris segmentation approach and recognition strategy which can exploit multiple features available for the potential identification. This paper presents an effective solution towards addressing such problem. The developed iris segmentation approach exploits random walker algorithm to efficiently estimate coarsely segmented iris images. These coarsely segmented iris images are post-processed using a sequence of operations which can effectively improve the segmentation accuracy. The robustness of the proposed iris segmentation approach is ascertained by providing comparison with other state-of-the-art algorithms using publicly available UBIRIS.v2, FRGC and CASIA.v4-distance databases. Our experimental results achieve improvement of 9.5%, 4.3% and 25.7% in the average segmentation accuracy, respectively for the UBIRIS.v2, FRGC and CASIA.v4-distance databases, as compared to the most competing approaches. We also exploit the simultaneously extracted periocular features to achieve significant performance improvement. The joint segmentation and combination strategy suggests promising results and achieves average improvement of 132.3%, 7.45% and 17.5% in the recognition performance, respectively from the UBIRIS.v2, FRGC and CASIA.v4-distance databases, as compared to the related competing approaches.*

1. Introduction

Automated iris recognition for distantly acquired images using visible imaging under less constrained conditions has received great attention recently [4]-[17]. Adoption of the visible imaging in the acquisition stage provides a few advantages over the conventional NIR-based iris recognition systems [18]-[22]. Such conventional acquisition setups operate in stop-and-stare mode which requires full cooperation from the subjects to provide images within close distance (1–3 feet) in order to ensure the acquired images are in good quality [1], [15] (i.e. the acquired images are in focus and have minimum acceptable iris diameter [2]-[3]). The constraints imposed in the conventional NIR-based iris recognition systems have limited the applicability of the iris recognition technology for forensic and surveillance applications, such as searching missing children and identifying terrorists from the crowd [6], [14]. Although recent NIR-based imaging technologies allow the farther reachable acquisition range (3m-8m) while controlling the NIR irradiance levels within the safety metrics [23]-[27], such systems are still not ideal to be practically considered for the forensic and surveillance applications. For example, [23]

requires subjects to walk through a portal to provide their iris images (see Figure 1(a)). In addition, the associated setup cost for such NIR-based long range iris acquisition system is relatively higher as compared to the visible imaging systems. The incurred cost may due to the additional devices such as the NIR illumination panels, band-pass filter and focus module, as the one shown in Figure 1(b).
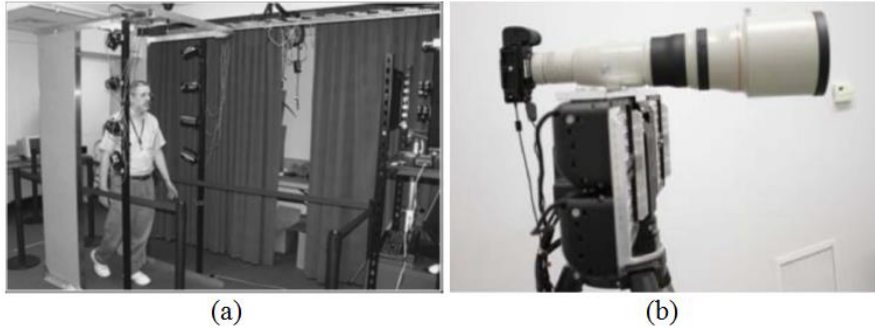

(a) (b)

Figure 1: Examples of long range iris acquisition systems: (a) portal of the "Iris on the Move" project [23], (b) iris acquisition system developed in [24] which is capable of acquiring iris images at distance up to 8 meters.

In contrast, visible imaging offers some advantages over the conventional NIR-based acquisition systems. NIR-based long range acquisition system must be cautiously designed and rigorously tested in order to ensure the irradiance levels meeting the specifications [26]-[27]. In such case, visible imaging acquisition provides better option as it is less constrained by such regulations due to the fact that human eyes are naturally responsive to the visible spectrum. In other words, strong illumination in visible spectrum will cause uncomfortableness to our eyes and therefore mechanistically responding with the actions such as blinking, pupil contraction and aversion [6], [14]-[15]. Significant advancement in the visible imaging technologies allow high resolution images to be conveniently acquired at-a-distance of 3m under less constrained conditions [14], [16]-[17] [51]. However the relaxation of rigid constraints as imposed in conventional NIR-based iris acquisition systems in the visible imaging context comes at a price. The acquired images are considerably noisier primarily due to the influence of multiple noisy artifacts, such as motion/defocus blur, occlusions from eyelashes, hair and eyeglasses, reflections, off-angle and partial eye images [8], [12], [14]. Therefore, development of robust and efficient iris recognition approaches which can work under such relaxed imaging constraints is highly desirable.

1.1 Related Work

Iris segmentation method reported in [7] employs a constellation model to perform the iris segmentation task. The constellation model places multiple integro-differential operators [3], [20] at the current evaluating pixel in order to find the local minimum score. The pixel found to be at local minimum will be employed in the next iteration. The process is then iterated until it converges or the predefined maximum number of iterations is reached. There are a few limitations observed in this method. Firstly, the segmentation model is still relying on the conventional segmentation approach which may not effectively segment the real-world acquired images. Secondly, the parameters for initial clustering pixels

2

must be carefully chosen as it will affect the performance of the subsequent segmentation operations. Thirdly, the constellation model may lead to a non-optimal iris center.

Approach [6] shows another promising effort in iris segmentation for the iris images acquired using visible imaging. Two neutral network classifiers were trained by exploiting local color features to classify image pixels into sclera/non-sclera and iris/non-iris categories. The trained classifiers operated in cascade order by firstly classifying sclera and then feeding the classified sclera pixels into the next classifier for iris pixels classification. Therefore, there exists a strong dependency between the two classifiers and any classification error from the first classifier will be propagated to the subsequent classifier which will eventually affect the segmentation accuracy. Furthermore, ref. [6] did not provide a complete automated framework to accommodate the situation when the face images are presented. Instead, the eye regions were manually cropped from the face images which are not sufficiently to model a more realistic case. In [14], localized Zernike features were exploited for classifying image pixels into either iris or non-iris category. In their approach, the Zernike features were computed for every single pixel which incurred heavily computational cost and therefore did not suitable to be considered for time sensitive applications.

Table 1: Summary of the Related Approaches

Ref.	Methodology	Feature		Automated Iris Segmentation	Iris Segmentation Complexity	Fusion	Operating Illumination		Focused Problem	
		Iris	Periocular				Visible illumination	NIR	Verification	Recognition
[6]	Iris segmentation using trained NN classifiers, Image features are from various color spaces	Yes	No	Yes	High	No	Yes (UBIRIS.v2, FRGC)	Yes (FERET, ICE2006)	No	No
[7]	Integral-differential constellation model	Yes	No	Yes	High	No	Yes (UBIRIS.v1 & v2)	No	No	No
[14]	Exploits local Zernike features and pixel-based classification using NN/SVM classifiers	Yes	No	Yes	Very high	No	Yes (UBIRIS.v2, FRGC)	Yes (CASIA.v4-distance)	Yes	Yes
[42]	Iris segmentation using Integral-differential operator while LBP is employed for periocular features	Yes	Yes	Yes	High	Yes	No	Yes (MBGC)	Yes	Yes
[43]	Iris segmentation is not performed while GIST and LBP are employed for *global* periocular features from whole image	No	Yes	No	N/A	No	Yes (UBIRIS.v2)	No	No	Yes
[44]	Periocular features using SIFT, LBP and HoG; No iris segmentation/ recognition or fusion with periocular information	No	Yes	No	N/A	No	Yes (FRGC, in-house acquired database)	No	Yes	Yes
[46]	Iris segmentation using commercial system. Periocular features using SIFT. No fusion of iris and periocular	Yes	Yes	Yes	High	No	No	Yes (MBGC 1.0 & 2.0)	Yes	Yes
This Paper	Random walk based unified iris and periocular segmentation; Improved iris recognition using LMF & DSIFT based periocular features/scores fusion	Yes	Yes	Yes	Low	Yes	Yes (UBIRIS.v2, FRGC)	Yes (CASIA.v4-distance)	Yes	Yes

N/A – Not applicable

Periocular features have invited increasing attention in biometrics and some promising efforts [42]-[44], [46] have been presented in the literature. Table 1 presents some of such related efforts in the literatures. A review on such (Table 1) related work suggests lack of efforts in developing a unified

approach that can simultaneously operates under visible and NIR images, which can be fully automated and adaptively exploits iris and periocular features for performance improvement. Such a strategy can also offer improved operational flexibility when one of the biometrics is degraded, missing or cannot be processed.

1.2 Our Work

The quality of the distantly acquired iris images, especially those under the visible imaging from the unconstrained environments, is usually degraded as compared to those employed in the conventional iris recognition systems. This poses several challenges in the development of robust iris segmentation and recognition approaches for such degraded images (noisy images). Therefore, this paper aims to provide a completely automated framework for remote iris recognition using such noisy images. The proposed solution can be broadly categorized into two parts: (1) segmentation and (2) recognition.

Efficient and robust segmentation algorithm is vital for any successful iris recognition strategy that can be deployed for online applications. In the segmentation part, the input image is firstly preprocessed for noise attenuation and image quality enhancement. The preprocessed image is then coarsely segmented using random walker algorithm followed by a sequence of post-processing operations to further refine the coarsely segmented result. The image is modeled based on the graph theory such that each pixel corresponds to the vertex (node) and the linkage between any two pixels corresponds to the edge of a graph. Such graph-based modeling allows the pixel-level segmentation as similar to [6], [14], so that iris segmentation can be performed regardless of iris size. Unlike the previous approaches [6], [14], the proposed method does not require to undergo extensive training[*] for either neural network or SVM classifier which can greatly reduce the computational cost in computing image features (see Section 3.2 for the discussion on the time complexity). Rigorous experiments were performed on three publicly available databases namely UBIRIS.v2 [5], [16], FRGC [36], [37] and CASIA.v4-distance [38] in order to ascertain the performance from the proposed segmentation framework. In addition to the significantly reduced computational complexity, the experimental results also illustrate marginal improvement in the average segmentation errors, *i.e.* to the extent of 9.5% and 4.3%, for the UBIRIS.v2 and FRGC databases respectively, while significant improvement up to 25.7% for the CASIA.v4-distance database, as compared to the most competing approach in [14].

Iris recognition performance for the noisy iris images still remains to be poor, despite with the use of the best segmentation strategy, *i.e.* as observed from the ideally segmented iris images using ground truth masks in our experiments (Section 3.3). Such poor performance for at-a-distance iris recognition has further motivated us to further incorporate additional/available features that are ignored while segmenting iris images. Therefore, the features around the eye region (periocular) which have been

---

[*] The only training involved is for the parameters optimization.

shown to be quite unique are exploited in this work to supplement the iris information. In this work, we consider two segmentation schemes for extracting the periocular region. The first scheme is referred as the *global* periocular region, which is the entire eye region[†] without performing segmentation and normalization. The second scheme is referred as *local* periocular region, which a localized region is extracted and normalized with respect to the segmented iris information. Texture analysis is then performed on both the extracted global and local periocular regions.

The matching scores from both iris and periocular features are firstly normalized using min-max normalization technique and then combined with the weighted sum technique. An average improvement of 52.4% in the rank-one recognition accuracy was observed from the experiments on the UBIRIS.v2, FRGC and CASIA.v4-distance databases, as compared to the most competing periocular features extraction methods in [43]-[44]. The main contributions of this paper can be summarized as follows:

- This paper has developed a significantly improved and computationally efficient approach for iris segmentation from the remotely acquired iris images under less constrained conditions. As compared to the existing competing iris segmentation approaches for the visible illumination images, the developed approach not only reduces the computational complexity (Section 3.2) but also achieves superior segmentation accuracy.

- The developed iris segmentation approach does not require rigorous training and therefore alleviates such mandatory complexity with the previous approaches [6], [14] for the training of statistical classifiers to perform the iris segmentation.

- Remotely acquired *visible illumination* eye images also illustrate discriminant periocular region which can be simultaneously exploited to improve the iris *recognition performance*. This paper presents such *joint strategy* to acquire multiple features and achieve superior performance. The experimental results are validated and compared on three publicly available databases, i.e. UBIRIS.v2 (visible), FRGC (visible) and CASIA.v4-distance (NIR), which illustrates superior performance, both in the identification and verification problems.

- This paper also presents comprehensive analysis of the global and local periocular regions to improve iris recognition from the visible and NIR illumination databases. The experimental results (Section 3.4) suggest superiority of combining global periocular details when discriminant features from the sufficient periocular regions can be segmented/extracted.

The remainder of this paper is organized as follows. In Section 2, the developed framework for simultaneously exploiting iris and periocular features is detailed. The experiments and performance evaluation are discussed in Section 3. Finally, conclusion is provided in Section 4.

[†] It is also referred to eye region detected by eye detector.

2. Iris and Periocular Segmentation from Less Constrained Acquired Face Images
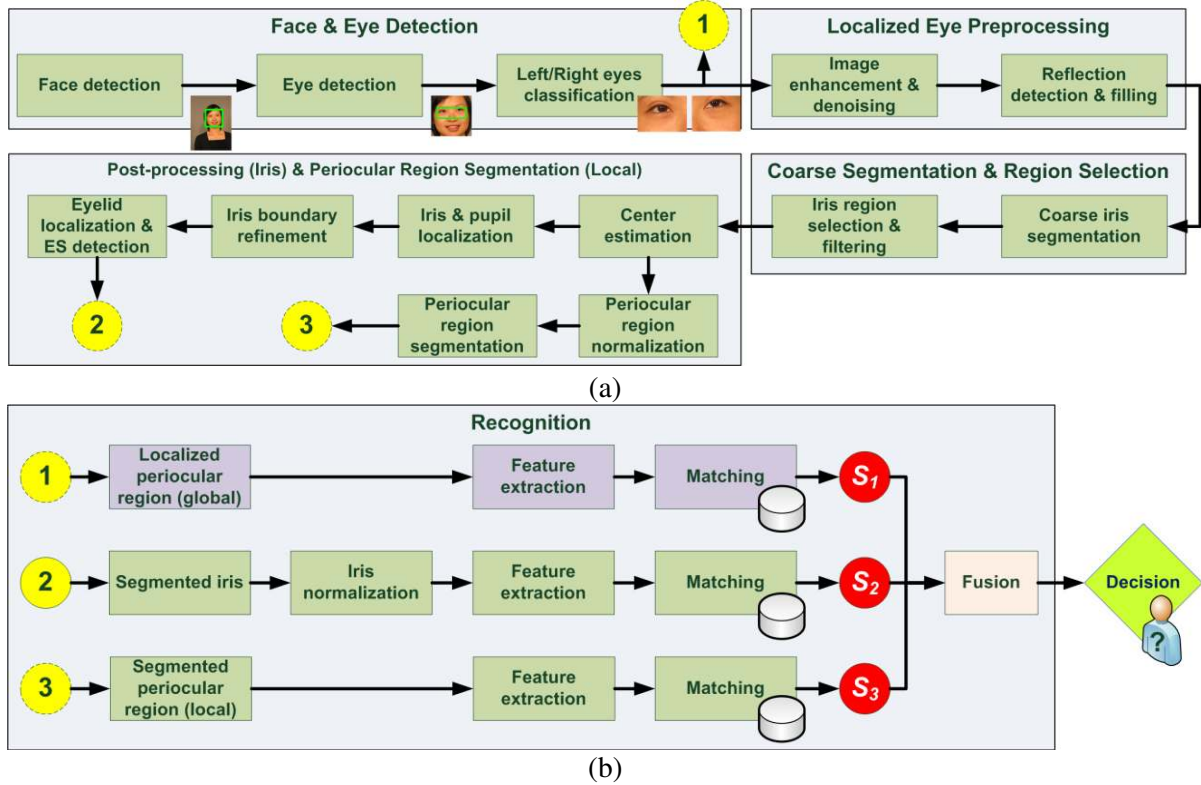

(a)

(b)

Figure 2: Block diagrams of the proposed multimodal recognition framework which generally consists of two parts: (a) Segmentation, (b) Recognition.

The proposed framework for jointly exploiting iris and periocular features from distantly acquired face images, under less constrained imaging environment, is shown in Figure 2. The proposed framework can be broadly categorized into two parts: part (a) is focusing on the segmentation of iris and periocular regions; while part (b) is concentrating on the human recognition utilizing the segmented information from part (a). In part (a), we employ the AdaBoost face and eye-pair detectors [‡] [34], [35] to automatically detect the face and eye-pair if face images are presented. Iris images are coarsely segmented using random walker algorithm and subjected to further refinement with a set of post-processing operations. Given the localized iris, the information such as iris center and radius can be approximated. Such information is employed to extract the periocular region and perform the scale normalization of the extracted region.

2.1 Preprocessing

[‡] Note that the objective of this paper is not to further improve the performance of face and eye detection but intentionally to present a completely automated iris recognition framework for distantly acquired images which can operate under real/varying imaging conditions.

Illumination variation is a common problem for imaging in real environment mainly due to the uncontrolled light source. Illumination variation not only poses difficulty in iris segmentation but also affects the recognition performance. Therefore, we adopt Retinex algorithm as detailed in [28]-[30] to address such problem. The algorithm provides high dynamic range compression which has been shown to be effective in improving the overall image quality, especially for those iris images acquired under real imaging conditions. After that, Gaussian filter with standard deviation $\sigma = 1.5$ is applied to the image in order to suppress high frequency contents in the acquired images and help in segmentation. Also, the reflection removal technique reported in [14] is adopted in order to mitigate the influence from the source reflection in the subsequence iris segmentation operations.

2.2 Coarse Iris Segmentation
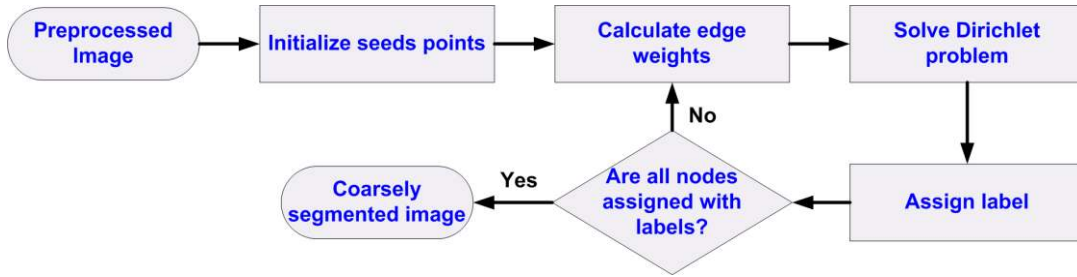
Figure 3: Flow chart of coarse segmentation using random walker algorithm.

The objective of the coarse iris segmentation is to provide a simplistic model to "*classify*" each image pixel into either iris or non-iris category. Such model is intended to provide the classification performance as close to the reported classification method in [14], but with significantly reduced computational cost and complexity. Although it is expected that such simplistic model may not produce classification result as good as to the statistically trained model [14], such limitation is addressed with the post-processing operations (see Section 2.3-2.7) which provide robust solution to further refine the coarsely segmented iris images.

In this work, random walker (RW) algorithm [31] is exploited to provide solution for obtaining the coarsely segmented binary iris mask B_c. The RW algorithm is a general interactive segmentation algorithm and the general procedure is illustrated in Figure 3. In RW algorithm, images are modeled based on the graph theory [32], such that image pixels corresponding to the vertices $v \in \mathbb{V}$ of an undirected graph $\mathbb{G} = (\mathbb{V}, \mathbb{E})$. An edge $e_{mn} \in \mathbb{E} \subset \mathbb{V} \times \mathbb{V}$ is attributed by two vertices v_m and v_n. Each edge is associated with a weight (cost), $\omega_{mn}(\omega_{nm} = \omega_{mn})$, and is calculated by exploiting the gradient information, i.e.:

$$\omega_{mn} = \exp(-\rho \mathcal{G}_{mn}{}^2), \tag{1}$$

where $\mathcal{G}_{mn}{}^2$ is the normalized square difference between the intensities at nodes m and n which can be calculated as follows:

7

$$\mathcal{G}_{mn}{}^2 = \frac{(g_m - g_n)^2}{\max\{o, p \in \mathbb{V}: e_{mn} \in \mathbb{E}\}(g_o - g_p)^2}. \tag{2}$$

The parameter ρ is the only free parameter which will affect the weighting function (eq. (2)).

The RW-based iris segmentation requires initialization of seed points which forms a subset of the labeled nodes $\mathbb{V}_l$, and the remaining unlabeled nodes are denoted as $\mathbb{V}_u$, such that $\mathbb{V}_l \cup \mathbb{V}_u = \mathbb{V}$. The $\mathbb{V}_l$ contains the nodes labeled as either foreground (+1) or background (-1), which constitute two initial models to estimate labels for $\mathbb{V}_u$. In order to provide automated initialization of seed points, the following rules are employed:

$$v_{l_k} = \begin{cases} +1 \text{ if } g_k < mod(I) - \varphi_f \sigma(I), \\ -1 \text{ if } g_k > mod(I) - \varphi_b \sigma(I), \\ 0 \text{ Otherwise } (v_{l_k} \in \mathbb{V}_u), \end{cases} \tag{3}$$

where $mod(I)$ and $\sigma(I)$ are the mode and standard deviation of input image I (preprocessed). The weights were empirically computed during the training phase and were set as $\varphi_f = \{1.6, 1.6, 1.6\}$ and $\varphi_b = \{0.7, 0.7, 1.25\}$, respectively for the UBIRIS.v2, FRGC and CASIA.v4-distance databases. Then the relationship between the labeled and unlabeled nodes can be expressed using Dirichlet integral, as follows:

$$I_D(\tilde{x}_u) = \frac{1}{2} \begin{bmatrix} \tilde{x}_l^T & \tilde{x}_u^T \end{bmatrix} \begin{bmatrix} L_l & B \\ B^T & L_u \end{bmatrix} \begin{bmatrix} \tilde{x}_l \\ \tilde{x}_u \end{bmatrix} = \frac{1}{2} \left(\tilde{x}_l^T L_l \tilde{x}_l + 2\tilde{x}_u^T B^T \tilde{x}_l + \tilde{x}_u^T L_u \tilde{x}_u \right), \tag{4}$$

where $\tilde{x}_l$ and $\tilde{x}_u$ denote the responses of the labeled and unlabeled nodes, respectively. L denotes the combinatorial Laplacian matrix defined as:

$$L_{mn} = \begin{cases} \sum_n \omega_{mn} \text{ if } m = n, \\ -\omega_{mn} \quad \text{ if } v_m \text{ and } v_n \text{ are adjacent nodes,} \\ 0 \quad \text{ otherwise.} \end{cases} \tag{5}$$

Nodes $\mathbb{V}_u$ are assigned with labels by solving the minimizer $\tilde{x}_u$ as in (6) iteratively.

$$L_u \tilde{x}_u = -B^T \tilde{x}_l. \tag{6}$$

2.3 Initial Iris Center Estimation

The iris image and the corresponding binary iris mask B_c obtained from the coarse iris segmentation stage are exploited to provide information in estimating the initial iris center. In [14], the initial iris center was obtained by measuring the center of mass of the classified iris mask, under the assumption that the classified iris mask is proximate to the actual iris region. However, the B_c obtained from the coarse segmentation stage may not always produce the iris mask which is proximate to the actual iris region. By directly measuring the center of masses from those B_c can cause serious deviation of the initial iris center from the actual one, as illustrated in Figure 4(a)-(c). More importantly, such measurement error will be propagated to the subsequence operations and affect the overall iris segmentation performance. Therefore, it is essential to refine the B_c in order to mitigate the influence

from the noisy artifact, or in particular, the eyelashes. As such, the mean of the heights μ_h from the masked region of B_c is employed to compute an adaptive threshold $\tau_h = 0.85 \times \mu_h$, which will be utilized to eliminate the column $h_g < \tau_h$, where h indicates the height of the column $g = 1, \dots, N$. The motivation to threshold the h_g is that the heights of the eyelashes regions beyond the iris region are observed to be shorter than the average height of the iris region, as shown from the third and the fourth sample images in Figure 4(d). The center of mass $C = (x_c, y_c)$ is then obtained from the refined binary mask $\tilde{B}_c$, as shown in Figure 4(e).
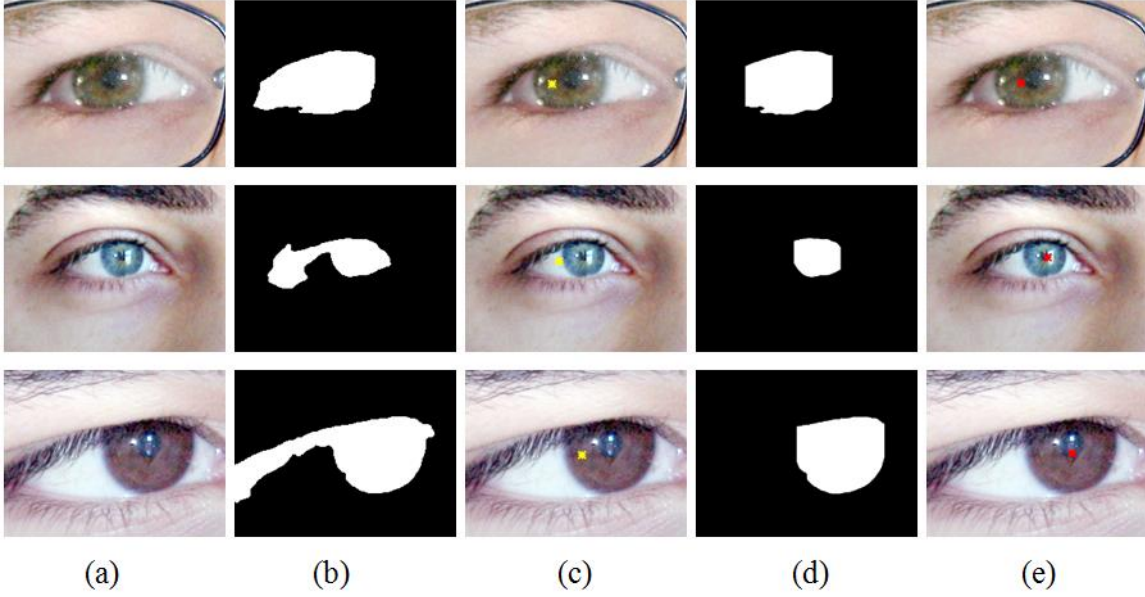
Figure 4: Initial center estimation, (a) Input enhanced image (color images are presented to provide better visualization), (b) Coarse segmented iris mask, (c) The estimated initial center (yellow mark) using (b), (d) Refined R_i, (e) The initial estimated iris center.

The C is obtained exclusively from the $\tilde{B}_c$, which does not exploit any of the underlying image feature such as the intensity/color information. Therefore, such additional intensity information will be exploited to further improve the accuracy of the initial estimation of the iris center. Similar as in [14], the red channel plane I_r of the input color image I is employed throughout the experiment. A 2D median filter with respective size of {7×7, 3×3, 9×9} for UBIRIS.v2, FRGC and CASIA.v4-distance is applied to I_r in order to smoothen the intensity variations across image pixels. After that, the smoothened I_r is subject to gamma correction, which takes the following mathematical form:

$$I_\gamma(x,y) = 255 \times \left(\frac{I_r(x,y)}{255}\right)^\gamma,$$

where I_γ is the gamma corrected of image I_r and (x,y) indicates the image coordinate. The γ is the parameter for gamma correction ($\gamma = \{0.8, 0.8, 1.0\}$ is empirically determined for three respective databases, i.e., UBIRIS.v2, FRGC and CASIA.v4-distance databases employed in the experiments). Given the refined mask $\tilde{B}_c$ and let's denotes $\boldsymbol{p_i} = (x_i, y_i)$ as the coarsely segmented iris pixels in $\tilde{B}_c$,

average intensity of a rectangular region of size $H \times H$ centered at $\boldsymbol{p}_i$ is then computed, where $H = 0.55 \times h_B$ and h_B denotes one half of the height of the bounding region of $\tilde{B}_c$. The region R_i which produces the minimum average intensity will be employed for further processing and other regions are ignored. It is to be noted that such refinement step narrows down the search region for estimating the initial center. The average intensity at each R_i can be computed using the intermediate image representation, i.e., integral image (see [35]), which allows the fast computation of the regional mean with just single image scan. Figure 5 illustrates the described refinement process and it can be observed from Figure 5(d) that the search region for estimating initial center has been reduced. By applying a weighted thresholding method $\tau_\omega = \omega \times \tau_{Otsu}$ to the localized region, a binary mask B_r is then generated. The τ_{Otsu} denotes the threshold obtained by using Otsu's thresholding method; the ω denotes the weight and is set to 0.65 for all the employed databases in the experiments. The center of mass $\tilde{C} = (x_{\tilde{c}}, y_{\tilde{c}})$ of B_r is then computed, as illustrated in Figure 5(e).

Both of the acquired centers C and $\tilde{C}$ provide the information to estimate the initial center and it is expected that C and $\tilde{C}$ should be close to each other. As such, the Euclidean distance between C and $\tilde{C}$ is measured, i.e. $d(C, \tilde{C}) = \sqrt{(x_c - x_{\tilde{c}})^2 + (y_c - y_{\tilde{c}})^2}$. The distance metric is employed in helping to make decision how should the acquired centers C and $\tilde{C}$ to be utilized, with the following rule applied:

Rule 1:

> If $d(C, \tilde{C}) > Threshold$
>   *Both C and $\tilde{C}$ are employed in the next operation.*
> *Else*
>   *Only C is employed in the next operation.*
> *End*

The distance threshold is set to 15 for all the employed databases. Note that all the presented parameters are empirically estimated using the training dataset (see Table 2), which is completely independent from the testing dataset.
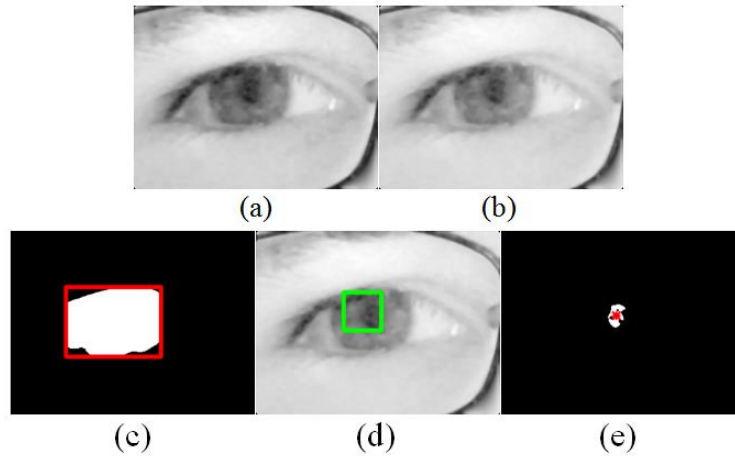

(a)   (b)

(c)   (d)   (e)

Figure 5: Initial center estimation using localized intensity information. (a) Extracted red channel plane, (b) Gamma corrected of image (a), with $\gamma = 0.8$, (c) The corresponding refined mask $\tilde{B}_c$ superimposed with a rectangle indicates the bounding region, (d) The region with the minimum average intensity, (e) Binary mask B_r and its center of mass. The estimated distance between C and $\tilde{C}$, $d(C, \tilde{C}) = 20.8945$.

2.4 Iris and Pupil Localization

The coarse segmented iris mask from the previous stage does not provide detailed information about limbic and pupillary boundaries, i.e., the radii of pupil and iris. By exploiting the information such as the coarse segmented iris mask B_c and the estimated center C from the previous stages, the limbic and pupillary boundaries will be approximated using circular model. Here, approximation to the limbic boundary shall be used as an example to illustrate the method and the localization of pupil boundary can be obtained in the similar manner[§]. The detailed steps of localizing the limbic boundary are as follows:

i. Firstly, an edge map E_m is obtained by applying Canny edge detector [33] to the smoothed image I_γ. The iris radius is obtained by searching the maximum response A using the formula (7):

$$A = \arg\max_{(x,y,r)} \sum_{n=0,\dots,N-1} E_m\left(p_n(x,y,r), q_n(x,y,r)\right), \tag{7}$$

$$x_c - \Delta o \leq x \leq x_c + \Delta o, \ y_c - \Delta o \leq y \leq y_c + \Delta o, \ \varphi_1\min(h_B, w_B) \leq r \leq \varphi_2\max(h_B, w_B): \varphi_1 < \varphi_2,$$

where x and y denote the coordinates within a bounding region calculated from the estimated center C and a predefined offset $\Delta o = \pm 15$. The r denotes the search radius which is calculated using the weighted half-height h_B and half-width w_B of the bounding region of $\tilde{B}_c$. The weights φ_1 and φ_2 are set to 0.7 (0.3) and 1.3 (0.8) for UBIRIS.v2 and FRGC (CASIA.v4-distance[**]) databases. The quantized N contour points (p, q) are calculated as $p_n(x, y, r) = r\cos\frac{2\pi}{N}n + x$ and $q_n(x, y, r) = r\sin\frac{2\pi}{N}n + y$ respectively.

ii. In case of two estimated centers are obtained from section 2.3, the step (i) is repeated for $\tilde{C}$, which yields $\tilde{A}$. Here, a simple heuristic is employed to check for the segmentation quality Q_s for both A and $\tilde{A}$, which can be computed as follows:

$$Q_s = \frac{A}{N}, \tag{8}$$

where N is the number of sampling points which acts as a normalization factor so that the $Q_s \in [0,1]$. The response which calculates the highest score will be employed and the other one is discarded.

[§] For NIR iris images, the order of localization is different, i.e. pupillary boundary is localized first then only followed by localizing limbic boundary.
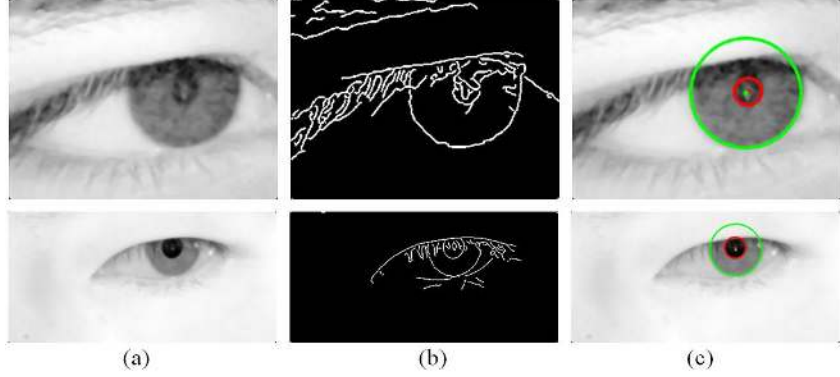[**] The weights are for localizing pupillary boundary as the order of localization is different for the NIR images.

Figure 6: Limbic and pupillary boundaries localization. (a) Input smoothed image I_r, (b) Edgemap of (a), (c) Localized limbic and pupillary boundaries.

The parameters which describe the limbic boundary (x_{ir}, y_{ir}, r_{ir}) should be obtained and are employed to approximate the pupillary boundary (x_{pu}, y_{pu}, r_{pu}). The (x_{ir}, y_{ir}) serves as the initial center and the predefined offset $\Delta o = \pm 10$. The search radius is calculated using r_{ir} with the weights φ_1 and φ_2 set to 0.2 and 0.6 for UBIRIS.v2 and FRGC databases. For localizing the limbic boundary of NIR-acquired iris images, we adopted different strategy for calculating the search radius, i.e. $\min(\varphi_1 r_{ir}, \varphi_1 \max(h_B, w_B)/2) \leq r \leq \varphi_1 \max(h_B, w_B)$, with $\varphi_1 = 1.3$. Figure 6 illustrates the described procedures for limbic and pupillary boundaries localization for both VW-acquired (first row) and NIR-acquired (second row) iris images.

2.5 Boundary Refinement

Iris segmentation for the iris images acquired under less constrained conditions is highly challenging. The simple circular model to approximate the limbic boundary as employed in Section 2.4 is not sufficient to accommodate the inherent image variations for the images acquired under such challenging environments. Therefore, boundary refinement approach as developed in this section aims to address for such limitation to further refine the localized limbic boundary as obtained from Section 2.4. Statistical intensity information is exploited from two defined regions R_1 and R_2 in order to compute the adaptive threshold to remove non-iris pixels near to the limbic boundary. Such two regions can be obtained with respect to the localized iris (x_{ir}, y_{ir}, r_{ir}) and localized pupil (x_{pu}, y_{pu}, r_{pu}) information. The region R_1 is defined as $R_1 = \{(x, y): x = r \cos \theta + x_{pu}, y = r \sin \theta + y_{pu}, r_{pu} < r \leq r_{pu} + \Delta o\}$. The offset Δo delimits the maximum size of the region to be considered, which is set to 20 for all the databases employed in the experiments. In order to mitigate the influence from the eyelid region which may potentially affect the performance, the lower part region of R_1 (half circular ring region) as illustrated in Figure 7(a), is considered. Mean μ_{R_1} and standard deviation σ_{R_1} are computed from such half-ring region to represent the statistical information of the iris region. An adaptive threshold is then calculated as $\tau_a = \mu_{R_1} + \beta \sigma_{R_1} : \beta \in \mathbb{R}, \beta > 0$, with the parameter β set to 2 for all the databases employed in the

experiments. The region R_2 can be obtained similarly as to R_1, with the $r_{ir} - \Delta o < r \leq r_{ir} + \Delta o$, as illustrated in Figure 7(b). The computed adaptive threshold is then applied to the I_γ, i.e. $I_\gamma > \tau_a$, and the pixels belong to R_2 are retained. The thresholded pixels can be considered as the outliers whose intensities are deviated to a certain degree from the statistical information of R_1. In order to improve the robustness of the algorithm, an additional constraint is imposed which only the connected pixels to the limbic boundary are retained. Note that our method is different from [7] which they considered the statistical information from two consecutive annular rings near the limbic boundary. The information near to the limbic boundary is observed to be unstable due to the poorly localized limbic boundary. As such, the developed approach exploits the statistical information from the half-ring region (R_1) near to the pupillary boundary for computing the adaptive threshold to refine limbic boundary. The half-ring region is considered to be more stable as it is less likely to be influenced from the eyelashes and eyelid region. Figure 7 presents two sample results of the proposed boundary refinement method obtained from two of the employed databases, i.e., UBIRIS.v2 (first row) and CASIA.v4-distance (second row).

(a)   (b)   (c)   (d)
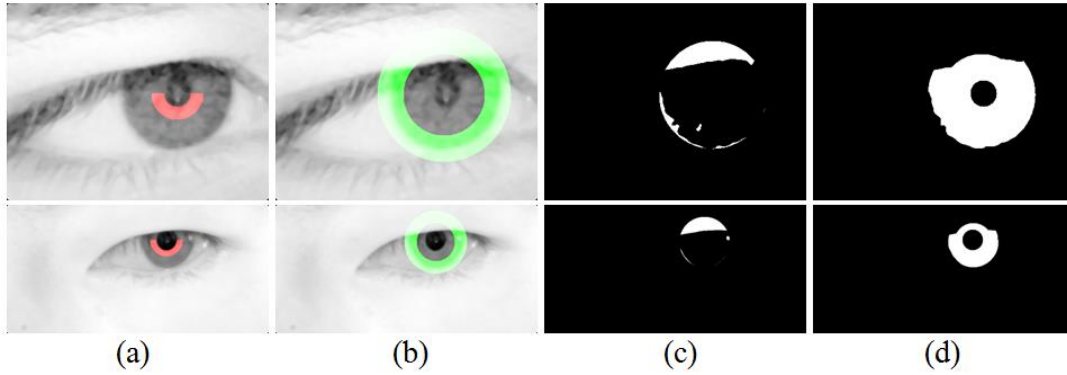
Figure 7: Boundary refinement. (a) Half-ring region R_1, (b) Region R_2, (c) Thresholded region, (d) Refined limbic boundary mask.

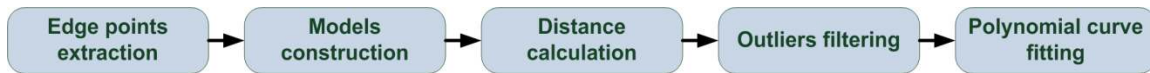**2.6 Eyelid Localization with Adaptive Eyelid Models**

Figure 8: Eyelid localization steps.

Figure 8 shows the procedure of the developed adaptive eyelid location approach. The localized limbic information $R_{ir} = (x_{ir}, y_{ir}, r_{ir})$ is employed to define the upper and lower eyelid regions. The upper eyelid region can be computed as follows:

$$R_{upper} = \{x, y: x_{ir} - r_{ir} \leq x \leq x_{ir} + r_{ir}, y_{ir} - r_{ir} \leq y \leq y_{ir} - 0.3 \times r_{ir}\}.$$

The edge points $\boldsymbol{p}_{k=1,\dots,K} \in (R_{upper} \cap R_{ir})$ within the intersection region of R_{upper} and R_{ir} (see Figure 9(b)) are extracted as the candidate points for the construction of the eyelid models. Three eyelid models $M_{l=\{/,^,\backslash\}}$ which represent the general eyelid shapes are adaptively constructed by exploiting the

13

information of the bounding region of $\boldsymbol{p}_k$. Each of the model requires three control points which can be obtained from the bounding region of $\boldsymbol{p}_k$, as defined as follows: $C_{M_/} = \{(x_{min}, y_{max}), (x_c, y_c), (x_{max}, y_c)\}$, $C_{M_\wedge} = \{(x_{min}, y_{max}), (x_c, y_c), (x_{max}, y_{max})\}$, and $C_{M_\backslash} = \{(x_{min}, y_c), (x_c, y_c), (x_{max}, y_{max})\}$. The x_{min}, y_{min} (x_{max}, y_{max}) denote the minimum (maximum) x- and y-coordinate of the bounding region while x_c, y_c denote the middle point of the bounding region. The three eyelid models are then constructed by applying a second degree polynomial interpolation to the calculated control points C_{M_l}, as illustrated in Figure 9(c)-(e). In order to measure the best representative eyelid model among M_l, $L1$ distance d_1 between $\boldsymbol{p}_k$ and $\boldsymbol{p}_{M_l}$ is firstly calculated. The model which produces the minimum d_1 is considered as the best representative eyelid model and is employed as a reference model to eliminate outlier edge points.
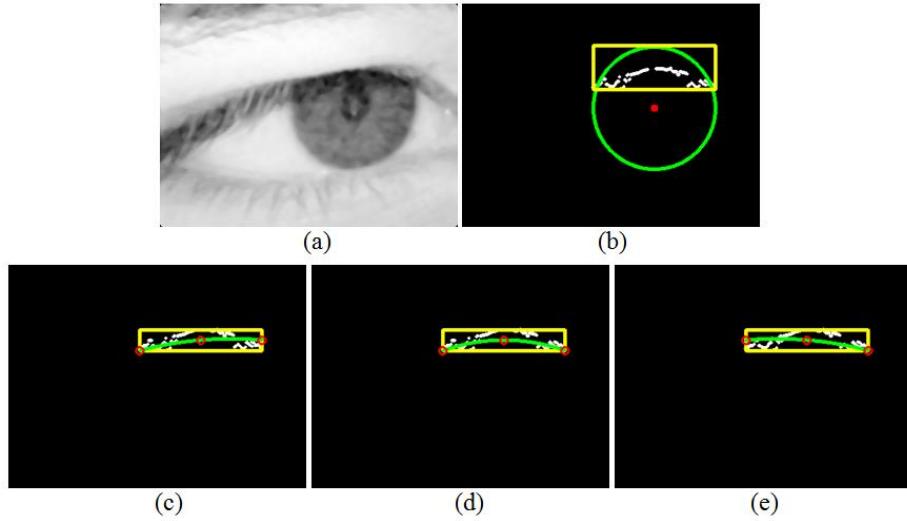
Figure 9: Adaptive eyelid models construction. Note that the edge points shown in the figures were enhanced for better visualization. (a) Input image, (b) Extracted edge points for upper eyelid from the delimited area, (c) Constructed upper eyelid model $M_/$ ($d_1 = 115.95$), (d) Constructed upper eyelid model $M_\wedge$ ($d_1 = 105.85$), (e) Constructed upper eyelid model $M_\backslash$ ($d_1 = 128.94$) (Note (c)-(e): Control points C_{M_l} are denoted using red 'o', bounding region is shown using yellow box and the constructed model is shown as green curve).

Let's denote $\mu_{\widetilde{d_{1k}}}$ and $\sigma_{\widetilde{d_{1k}}}$ respectively as the mean and standard deviation of the distance $\widetilde{d_{1k}} = |\boldsymbol{p}_k - \boldsymbol{p}_{M_{lk}}|$ between the nominated eyelid model and the $\boldsymbol{p}_k$. Outlier edge points can be detected by performing the following statistical test:

$$\epsilon_k = \frac{\left(\widetilde{d_{1k}} - \mu_{\widetilde{d_{1k}}}\right)^2}{\sigma_{\widetilde{d_{1k}}}^2}. \tag{9}$$

The edge point $\boldsymbol{p}_k$ whose $\epsilon_k > 3$ is considered as the outlier point and is excluded for the subsequent operation. A second degree polynomial curve is fitted to the remaining candidate edge points in order to eliminate the non-iris region (upper/lower eyelid region). Figure 10 presents some sample results obtained from the developed eyelid localization technique. Localization of the lower eyelid region can be

performed similarly as to the upper eyelid region. The proposed eyelid localization using adaptive eyelid models is inspired by the work in [18] which three representative eyelid models were trained for each upper and lower eyelid to eliminate the outlier points. One of the advantages of the proposed localization method is required no prior training for the eyelid models while providing the similar functionality as in [18] to regulate the extracted edge points. The eyelid models are adaptively constructed by exploiting the localized information from each segmented iris and therefore provide superior localization capability than the globally trained models.
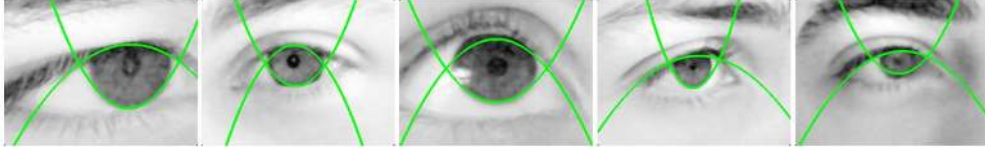
Figure 10: Sample eyelid localization results obtained using the adaptive eyelid model.

2.7 Eyelashes and Shadow Masking
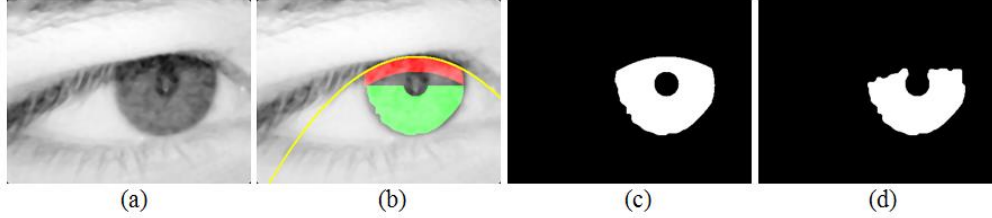
Figure 11: Eyelashes and shadow masking. (a) Input image, (b) ES (red) and IR (green) regions, (c) & (d) Iris masks before and after the ES masking, respectively.

Eyelashes and shadow (ES) are one of the commonly observed noisy artifacts which occlude portion of iris region. The proposed ES masking method is similarly as to [14] by exploiting statistical information of the localized iris region to detect those noisy pixels. Firstly, the localized iris region is virtually divided into two regions namely ES region and IR region. ES region is defined as the region calculated from the localized upper eyelid to a distance $d = 0.3 \times r_{ir}$ while IR region is defined as the lower half annular region of the localized iris, as illustrated in Figure 11(b). Mean $\mu(\text{IR})$ and standard deviation $\sigma(\text{IR})$ of the IR region which describe the intensity distribution of the localized iris region are calculated. Such information is then employed to calculate two adaptive thresholds: $\tau_{low} = \mu(\text{IR}) - \delta_1\sigma(\text{IR})$ and $\tau_{high} = \mu(\text{IR}) + \delta_2\sigma(\text{IR})$, with the weights set to $\delta_1 = 3.5$ and $\delta_2 = 2.5$. The computed thresholds are employed to detect noisy pixels within ES region whose intensity $I < \tau_{low}$ or $I > \tau_{high}$. In addition, the τ_{high} serves as the complementary to the Section 2.6 to further eliminate eyelid pixels which may not be successfully removed in the earlier operation. Figure 11 illustrates the described ES masking method and it can be observed that the proposed method was effectively eliminated outlier pixels within the ES region.

2.8 Segmentation of Periocular Region

Periocular is referred to the region around the eye [44]. Currently, there is no clear definition about what the size of the periocular region should be, e.g. ref. [44], [46] use the periocular region which is quite different from the [43]. However, the automated segmentation of periocular region, e.g. those in [44], [46], is more challenging in less constrained imaging environment as the size of the periocular region is highly dependent on the distance between subjects and the camera. Ref. [44] provides a promising solution to address such issue which the authors suggested to utilize the localized iris as a reference for segmenting the periocular region. Scale and translation-invariant are achieved by employing segmented iris information (x_{ir}, y_{ir}, r_{ir}) as a reference to normalize and segment the periocular region. Firstly, the input image is normalized (upscaling/downscaling) w.r.t the scale factor, $s_f = {r_{norm}}/{r_{ir}}$, where r_{norm} corresponds to the normalized iris radius. The normalization operation results in shifting of the iris center (x_{ir}, y_{ir}) in the scaled image I_{S_f}, and the updated iris center can be calculated as $(\widetilde{x_{ir}}, \widetilde{y_{ir}}) = s_f(x_{ir}, y_{ir})$. The periocular region R_{pe} is then defined as the rectangular region of size $\grave{w} \times \grave{h}$ centered at $(\widetilde{x_{ir}}, \widetilde{y_{ir}})$. The $\grave{w}$ and $\grave{h}$ correspond to the width and the height of R_{pe}, which can be calculated as $\grave{w} = r_{norm} \times f_w$ and $\grave{h} = r_{norm} \times f_h$, respectively. The factors f_w and f_h are fixed for all the images on the same dataset to ensure the consistent size of the R_{pe} to be segmented. We set $f_w = \{6,6,8\}$ and $f_h = \{4,4,6\}$ respectively for the UBIRIS.v2, FRGC and CASIA.v4-distance databases. Figure 12 shows the sample normalization and segmentation results of the periocular region from the same subject.
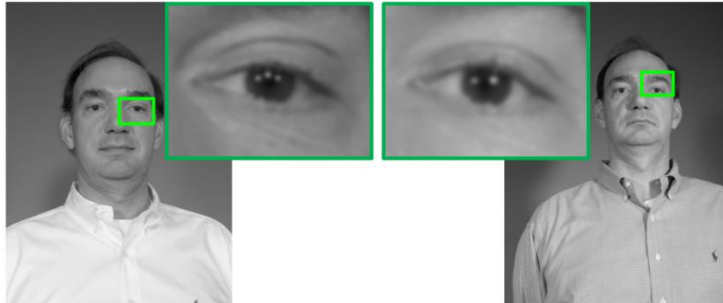

Figure 12: Segmentation and normalization of the periocular region from face images acquired at-a-distance (left eyes are employed for better illustration and comparison).

3. Experiments and Results

3.1 Databases

Three publicly available databases namely: (a) UBIRIS.v2 [5], (b) FRGC [36], and (c) CASIA.v4-distance [38] were employed to evaluate the performance of the proposed method. The images from the first two databases were distantly acquired using visible imaging while the images from the third database were acquired using NIR imaging. Table 2 provides summarized information about the employed databases for the conducted experiments.

Table 2: Overview of the three employed databases

	UBIRIS.v2	FRGC	CASIA.v4-distance
Imaging system	visible	visible	NIR
Acquisition distance (m)	4 - 8	N/A	≥3
Original image size	400×300	1200×1600	2352×1728
No. of train images / subjects	96 / 19	40 / 13	79 / 10
No. of test images / subjects	904 / 152	500 / 150	502 / 67 (995 / 131)*

(*) denotes different numbers of images / subjects employed in the evaluation of recognition performance

a. **UBIRIS.v2**: The full database consists of a total of 11102 images from 261 subjects. The images were acquired under unconstrained conditions with subjects at-a-distance and on the move. The standoff distance (distance between subject and the camera) spanning from 4 to 9 meters. As similar to [14], only subset of the images was employed in the experiment. The subset consists of 1000 images from 171 subjects. Images of the first 19 subjects were employed as train images for parameters training and the rest of 904 images were employed as test images[††].

b. **FRGC**: The images from the high resolution still images category were considered in our experiments. As similar to [14], only subset of images was employed. The subset images were selected from the session 2002-269 to 2002-317 of Fall 2002. We employed the same procedure as reported in [14] for automatically localizing eye regions from these subject images.

c. **CASIA.v4-distance**: The full database consists of a total of 2567 images from 142 subjects. The images were acquired using NIR imaging with the subjects 3 meters away from the camera. Images from the first 10 subjects were employed as train images. For test images, images from the subjects 11 – 77 were employed in evaluating segmentation performance while images from the subjects 11 – 141 (i.e., all subjects exclusive the train images) were employed in evaluating recognition performance. Note that only the *first eight left/right eye* images were considered in the experiments.

3.2 Segmentation Accuracy and Complexity

Performance of the proposed iris segmentation method was evaluated using the protocol as adopted in NICE.I competition [16]. The average segmentation error, $\overline{E_1}$ is given as:

$$\overline{E_1} = \frac{1}{N \times c \times r} \sum_{c' \in c} \sum_{r' \in r} O(c', r') \otimes C(c', r'), \tag{10}$$

where O and C respectively correspond to the ground truth[‡‡]and segmented iris masks, c and r denote the total numbers of columns and rows of the image; N is the total number of images. The XOR operator '$\otimes$' served to evaluate the disagreeing pixels between O and C. The proposed iris segmentation method reports average segmentation errors of 1.72%, 1.76% and 0.81% on *UBIRIS.v2*, *FRGC* and *CASIA.v4-*

[††] All the employed train images were independent from the test images.
[‡‡] Ground truth masks for the three employed databases are available from [39].

distance databases§§. The improvement over the method reported in [14] was respectively 9.5%, 4.3% and 25.7% on these three databases. Comparison is also performed against other state-of-the-art methods [6], [7], [14], [19], [40], [41], as summarized in Figure 13. This figure also illustrates statistical significance of the performance improvement over respective state-of-art approaches (p-value at significance level of $\alpha = 0.05$ using independent two-sample test technique [54]). It can be observed that the proposed segmentation method outperforms the methods [6], [7], [14], [19], [40], [41] for UBIRIS.v2 and FRGC databases. The improvement over [6], [7], [14], [19], [40] can also observed for the experiment on CASIA.v4-distance database. The approach [41] reports similar average segmentation error as the develop approach. Note that approaches [40], [41] employ the post-processing operations as developed in this paper (Section 2.3 – 2.7) to further refine the coarsely segmented iris images. The robustness of the developed post-processing operations is further ascertained from the competitive segmentation performance obtained for the approaches [40], [41]. The proposed segmentation technique not only achieved better segmentation accuracy but also has the advantage in time efficiency. Table 3 summarizes the comparison of the average execution time for computation of image features in the segmentation stage. All the implementations were performed in Matlab environment and executed on Intel 2.93 GHz processor with 4 GB RAM. Figure 14 shows some sample segmentation results obtained from the three employed databases. As can be observed from Table 3, the proposed segmentation technique significantly reduced the computational complexity in performing the iris segmentation. In [14], localized Zernike features are computed for every single pixel, which may explains the reason why significant amount of time is required.
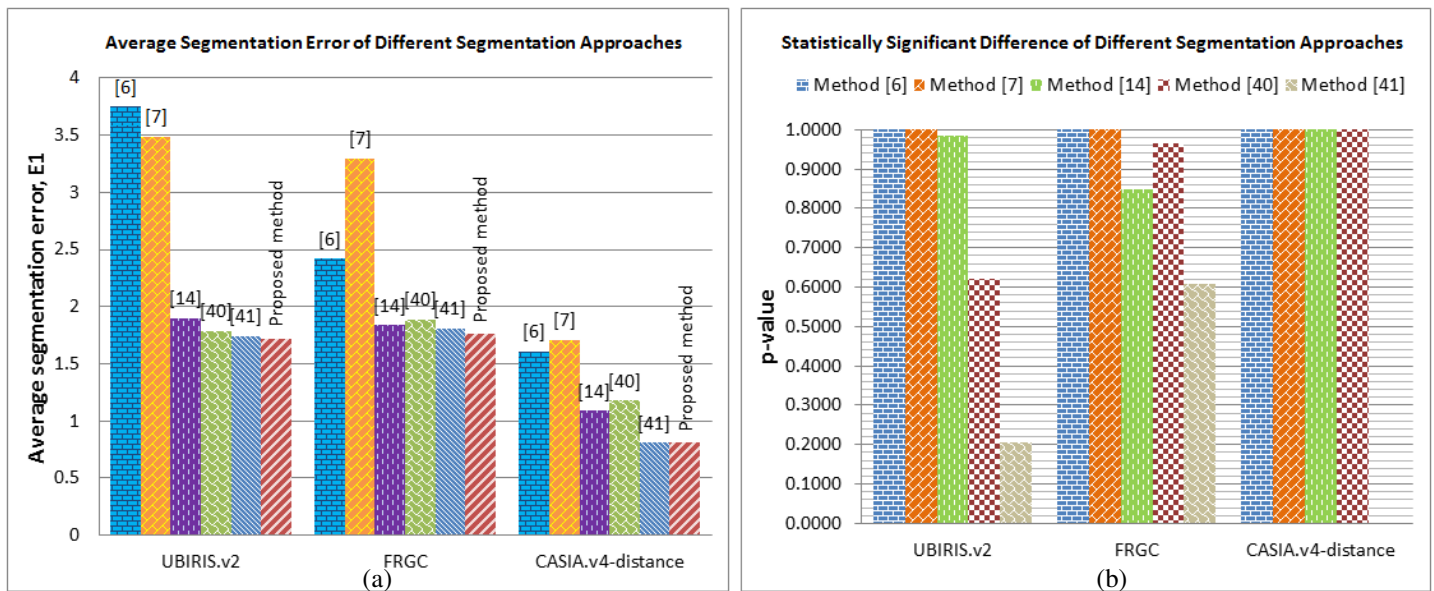

Figure 13: Performance of the iris segmentation methods. (a) Average segmentation error ($\overline{E_1}$), (b) Statistically significant difference of different segmentation approaches as compared to the proposed method.

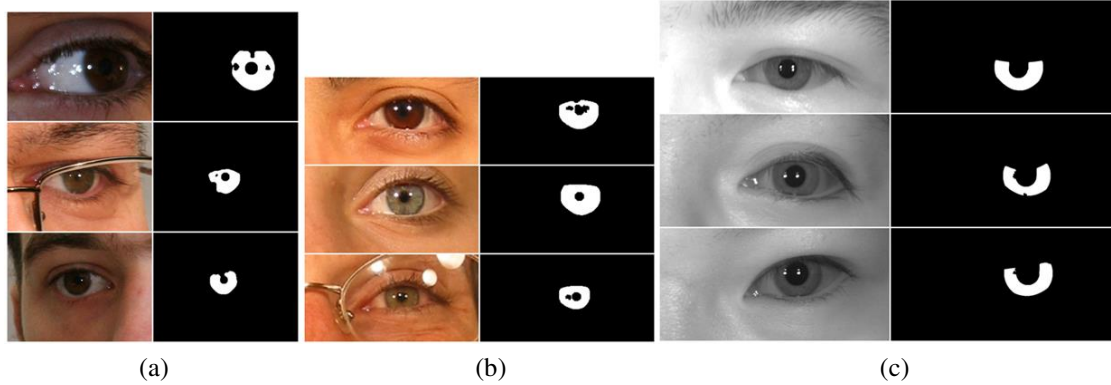§§ The results will be presented in this order unless otherwise specified.

| | (a) | (b) | (c) |

Figure 14: Sample segmentation results on (a) UBIRIS.v2, (b) FRGC, (c) CASIA.v4-distance.

Table 3: Average execution time

	Average Execution Time (second)		Improvement (%)
	Method [14]	Proposed method	
UBIRIS.v2	136.3	0.75	99.4
FRGC	51.1	0.39	99.2
CASIA.v4-distance	368.2	1.53	99.6

3.3 Iris Recognition Accuracy

The segmented iris image is firstly normalized into a predefined size[***] based on the rubber sheet model as proposed in [3], [20] to make the segmented iris image invariant to the pupillary dilation/constriction and the iris size. For iris feature extraction, log-Gabor filter [22] with the parameters as in [14] is employed. The recognition results for both the databases acquired using visible imaging (UBIRIS.v2 and FRGC) are poor and not encouraging. In order to investigate into such matter, the iris recognition performance for the ideally segmented cases (i.e. iris segmentation using the ground truth masks [39]) is employed as baseline to benchmark the recognition performance of the developed iris segmentation approach, as shown in Figure 15 and 16. The reported recognition performance suggests that the poor recognition performance may not be entirely attributed to the poorly segmented iris images.

| (a) | (b) |
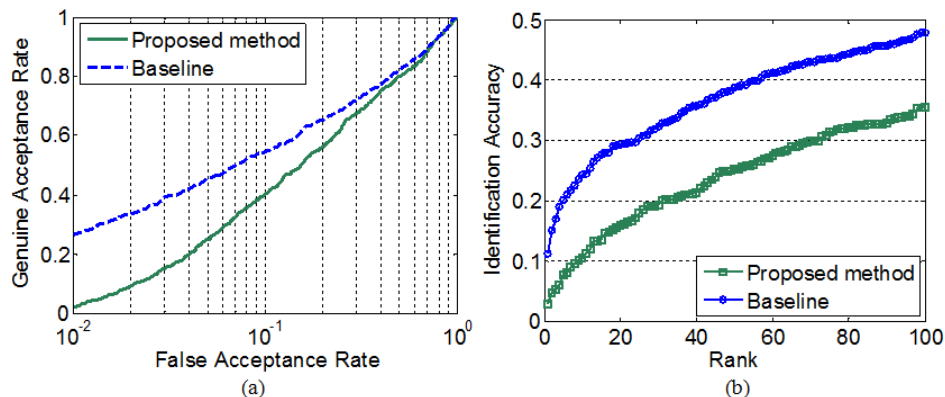
Figure 15: Iris recognition performance for UBIRIS.v2 database. (a) ROC and, (b) CMC for the proposed method and the baseline.

[***]The normalized templates for the segmented images from the UBIRIS.v2, FRGC and CASIA.v4 are 512×64, 256×32 and 512×64 respectively.
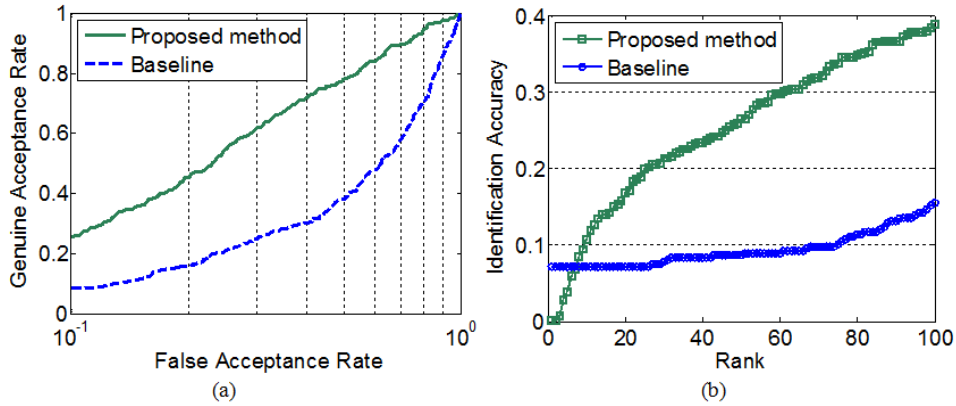
Figure 16: Iris recognition performance for FRGC database. (a) ROC and, (b) CMC for the proposed method and the baseline.

Figure 17: Iris pigmentation. (a) Darkly pigmented iris, (b) Lightly pigmented iris.
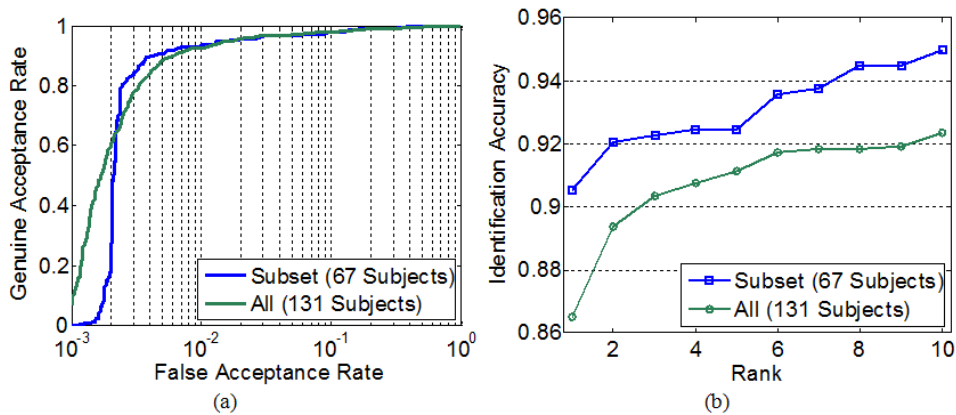

Figure 18: Iris recognition performance for developed method on CASIA.v4-distance database. (a) ROC and, (b) CMC.

Such discouraging recognition performance may due to the fact that noise level influencing the visible illumination images is significantly higher (highly degraded image quality) than the iris images acquired under rigidly constrained environment. In addition, although human eye has higher sensitivity to the visible light, complex iris patterns for darkly pigmented iris can hardly be revealed using visible spectrum [47], [1], [6], as depicted in Figure 17. On the other hand, the recognition performance for distantly acquired iris images using NIR imaging is observed to be significantly better than those

observed for acquisition using visible imaging, as shown in Figure 18. For such database, the rank-one identification rate achieved 90.5% when only subset of the images (67 subjects employed in evaluating segmentation performance) was employed. The identification rate read 86.5% when the first eight images from all the subjects (141 subjects) were employed in the experiments.

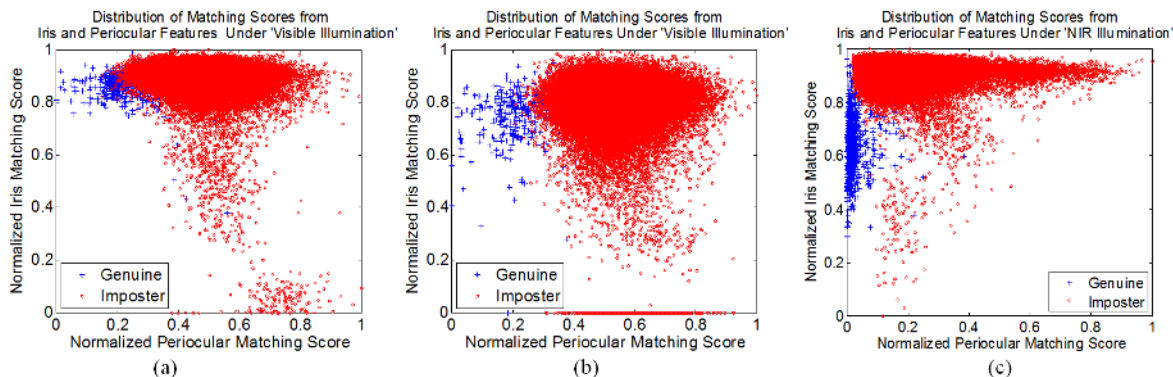### 3.4 Combining Iris and Periocular Features Matching Scores

Figure 19: Distribution of matching scores from iris and periocular features for (a) UBIRIS.v2, (b) FRGC, (c) CASIA.v4-distance.

Joint strategy maybe provides the solution to improve the recognition performance for such noisy images. Periocular region is of particular interest in this paper as such region is usually simultaneously acquired with the eye without incurring additional hardware cost. Several promising efforts such as [42]-[44], [46] have shown encouraging recognition performance by employing the periocular region. As such, rigorous experiments were carried out in this paper to further investigate recognition performance using joint strategy at score level. The employed joint strategy combines the simultaneously acquired iris and periocular matching scores based on the weighted sum rule. In this paper, several commonly employed feature extraction approaches such as SIFT [49], [50], GIST [47], LBP [52], HoG [53] and LMF (Leung-Malik Filters) [48] were exploited for computing periocular features. Two types of the experiments: Experiment I and II were carried out to rigorously evaluate those periocular feature extraction methods (as elaborated below). The detailed procedure of the best performing feature extraction approach obtained from the Experiment I and II is then provided. Figure 19 shows the distribution of the simultaneously generated genuine and imposter scores for UBIRIS.v2, FRGC and CASIA.v4-distance. The periocular scores in this figure were generated using the best performing DSIFT and LMF features (Experiment I & II). The distribution of genuine and imposter scores in Figure 18 suggest that there may exist complementary information from the iris and periocular, which can be jointly exploited. Such joint strategy is expected to achieve superior recognition performance that may not be possible by using either iris or periocular. The combination of the scores obtained from the multiple periocular features was also analyzed before performing the comparison with some of the existing competing approaches for the periocular biometrics.

- ***Experiment I:*** The segmented periocular region R_{pe} (see Section 2.8) was employed in experiment I. Such segmented region is referred as *local* periocular region in this paper. The experimental results from the three employed databases for the fusion of scores obtained from the *local* periocular and iris features are shown in Figure 20-22. The best of the rank-one recognition rates of *39.6%* and *53.2%* were observed for the joint scores obtained from the periocular (dense SIFT / DSIFT) and iris features on the UBIRIS.v2 and FRGC databases respectively. For CASIA.v4-distance database, the best rank-one recognition rate was observed to be *93.2%* for the fusion of the scores obtained from the periocular (LMF) and iris features. However, joint score obtained from the periocular (DSIFT) and iris features was observed to provide an overall best recognition performance on the CASIA.v4-distance database, with marginal decrement of *0.3%* in the rank-one recognition rate.
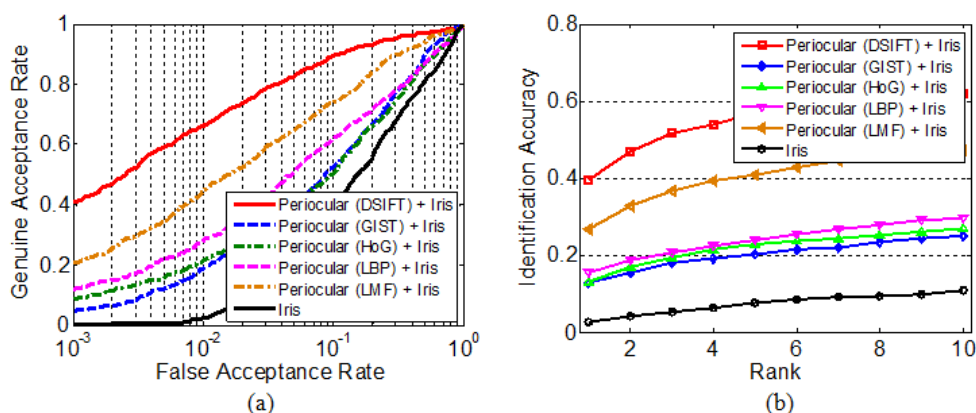
Figure 20: Recognition performance for the score fusion from the periocular and iris features for UBIRIS.v2 database. (a) ROC, (b) CMC.
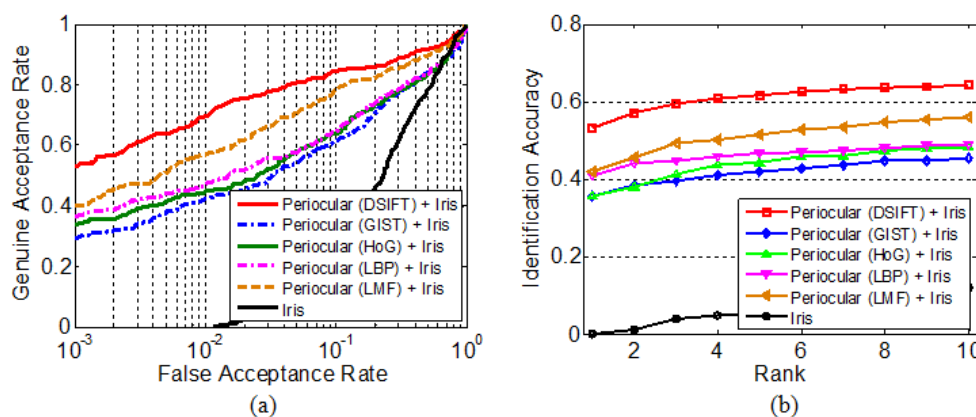

Figure 21: Recognition performance for the score fusion from the periocular and iris features for FRGC database. (a) ROC, (b) CMC.
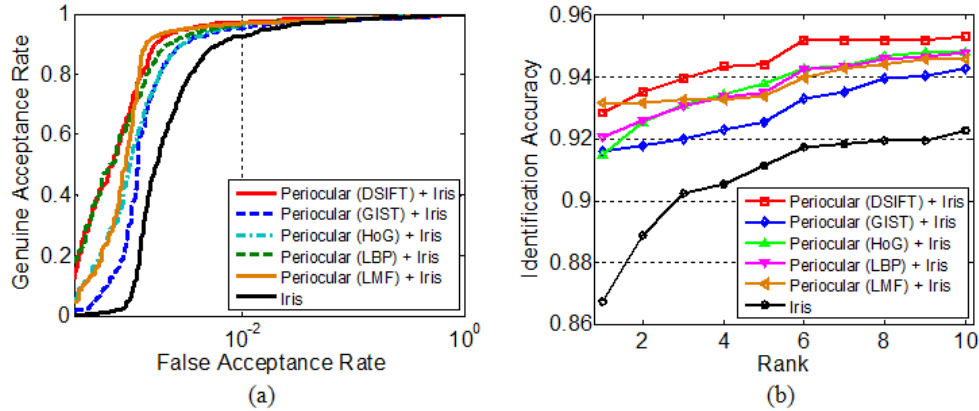
22

Figure 22: Recognition performance for the score fusion from the periocular and iris features for CASIA.v4-distance database. (a) ROC, (b) CMC.

- *Experiment II*: In [43], periocular features were directly computed from the localized eye region (the detected eye region) without involving segmentation step as described in Section 2.8. Therefore, the periocular region is considered as the immediate region detected by the eye detector[†††], which is referred as the *global* periocular region in this paper. Such global periocular region is particularly useful if the iris segmentation fails or the quality of the segmented iris image do not meet the minimum requirements. Unlike the local periocular region, the size and the location of the global periocular region is less consistent as such region is highly dependent on the detected eye region. For that reason, experiment II was carried out to objectively evaluate the performance of the various feature extraction methods [47]-[50], [52]-[53] for the global periocular region. The experimental results for the fusion of the scores obtained from the global periocular and iris features on the three employed databases are respectively shown in Figure 23-25. The best recognition performance is observed for the score combination from the periocular (DSIFT) and iris features on the UBIRIS.v2 and FRGC databases, which respectively reports the rank-one recognition rate of 39.4% and 59.9%. As compared to the experiment I, the achieved rank-one recognition rate reports an improvement of 12.6% for the experiment using FRGC database. In contrast, a 18% decrement on the rank-one recognition rate is observed as compared to the experiment I for the combination of global periocular (DSIFT) and iris features on the URIBIS.v2 database. For the experiment using CASIA.v4-distance database, the best recognition performance is observed for the score fusion of periocular (LMF) and iris features, which reports the rank-one recognition rate of 93.9%.

- *Periocular feature extraction:* Promising recognition performance using periocular and iris features have been ascertained through the experiment I and II. Therefore, the procedure of the best performing periocular feature extraction methods, i.e., DSIFT and LMF are further detailed in this

---

[†††] Note that the UBIRIS.v2 provides the localized eye images and therefore eye detection is not required for the images from this database.

paper. Figure 26 illustrates the general training and the matching processes for the periocular biometrics using either DSIFT or LMF as features. During the training phase, a k-texton dictionary is constructed. Given the M training images, DSIFT/LMF features are computed from the periocular region (local/global) of each training image. The texton dictionary is then constructed by clustering the computed M DSIFT/LMF feature vectors using k-means clustering approach. In order to select the best k representative textons, a discrete set of k-values was evaluated for both DSIFT and LMF methods, as shown in Figure 27. In the matching process, the periocular features are extracted similarly as in the training process. The extracted periocular features are then classified using the trained texton dictionary and number of occurrences of each classified texton is computed to form a k-bin histogram. Matching score between two templates is computed using the Chi-square distance.
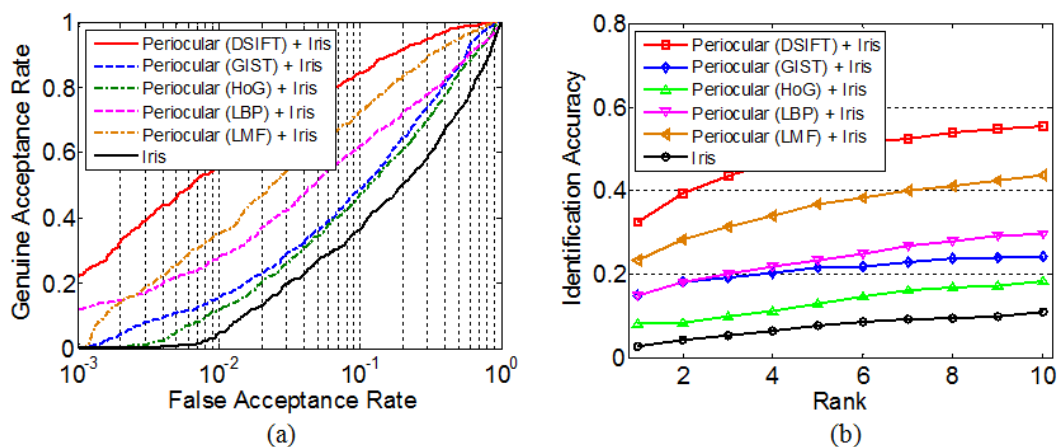

Figure 23: Recognition performance using the joint score from the periocular and iris features for UBIRIS.v2 database. (a) ROC, (b) CMC.
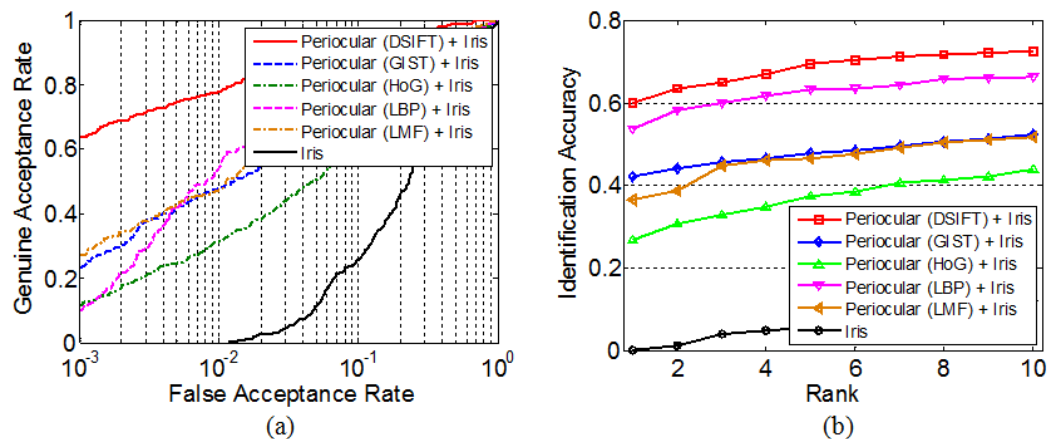

Figure 24: Recognition performance using the joint score from the periocular and iris features for FRGC database. (a) ROC, (b) CMC.
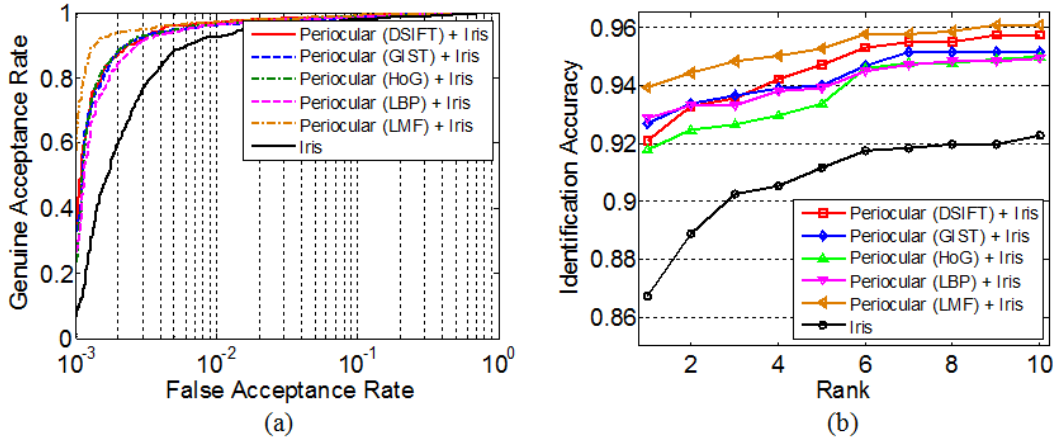
Figure 25: Recognition performance for the score fusion of the periocular and iris features for CASIA.v4-distance database. (a) ROC, (b) CMC.
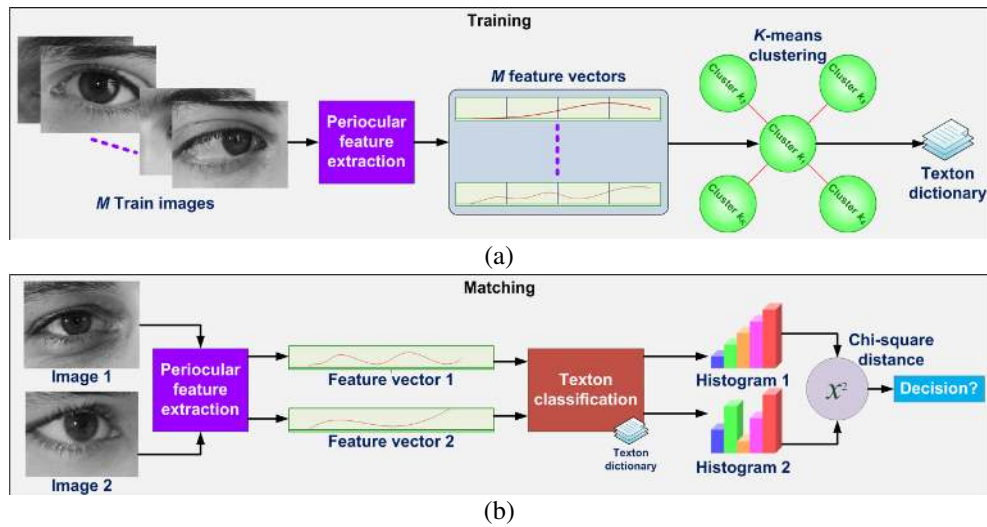

(a)

(b)

Figure 26: Illustration of periocular training and matching processes: (a) training of texton dictionary, (b) Example of matching process.
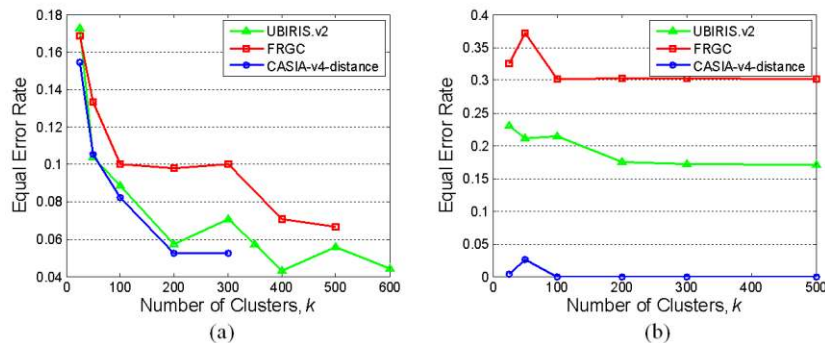

Figure 27: Training of parameter k for clustering the best k textons using (a) DSIFT, (b) LMF features.

- *Score fusion:* The matching scores for the periocular and iris features are computed based on two different score systems. Therefore, score normalization is performed prior to the score fusion. The min-max normalization technique is employed for such purpose to normalize the matching scores

computed from the periocular and iris features. The normalized scores are combined using the weighted sum rule.
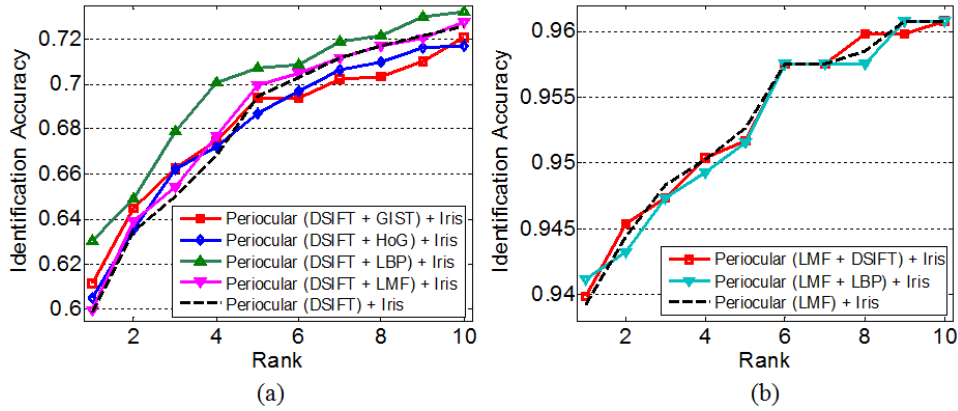

Figure 28: CMCs for the fusion of multiple features. (a) FRGC, (b) CASIA.v4-distance.

- *Joint scores from multiple features:* Joint scores obtained from multiple features were also exploited in this paper. The recognition performance for the experiments on FRGC and CASIA.v4-distance databases are shown using the CMC curves in Figure 28. The recognition performance for the experiment on UBIRIS.v2 is not provided as no significant improvement was observed for the score combination from the multiple features. The improvement in rank-one recognition rates is observed to be 5.3% and 0.2% respectively for the FRGC and CASIA.v4-distance databases when score fusion from multiple features was employed.

- *Comparison with existing methods:* Previous approaches as reported in [43] and [44] compute multiple periocular features and exploit the score fusion of the computed features to improve the recognition accuracy. The best performing joint strategy obtained from the experiments as described earlier is compared with the competing approaches [43] and [44], as shown by the CMC curves in Figure 29. The recognition performance of each considered periocular feature in the best performing joint strategy is also provided. Such joint strategy suggests that they may exist complementary information from multiple periocular and iris features which can be exploited to achieve superior recognition accuracy. An overall improvement of 52.4% in rank-one recognition accuracy was observed, as compared to the methods [43] and [44]. It can be noticed that the experimental results obtained from the UBIRIS.v2 database achieved the lowest accuracy among all the employed databases. One of the possible reasons to explain for such discouraging performance may due to the lack of sufficient periocular regions for better feature representation. The localized eye images provided from the UBIRIS.v2 database do not have sufficient periocular regions (e.g. eyebrow, malar fold, nasojugal fold, etc.) as compared to FRGC and CASIA.v4-distance databases. Figure 30 provides several sample images from each of the employed databases. As can be observed from such figure, sufficient periocular regions

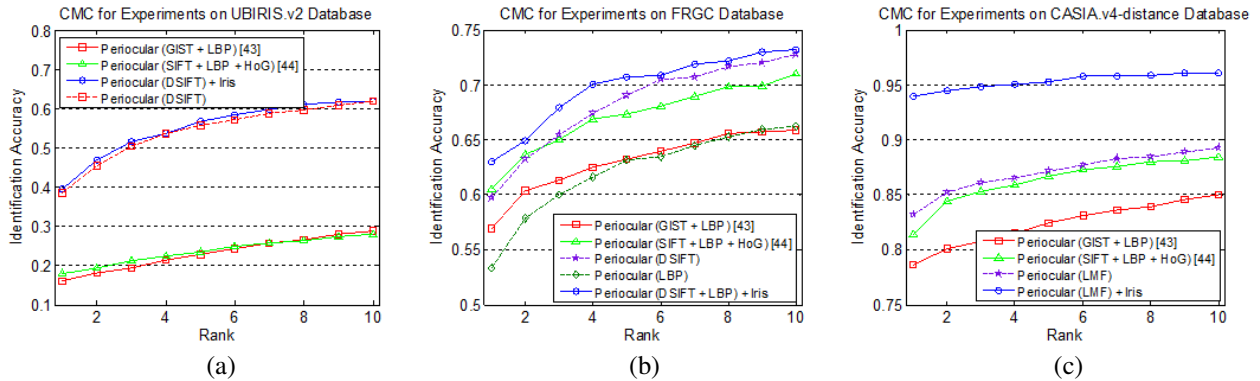can be extracted from the face (or partial face) images provided in FRGC and CASIA.v4-distance databases.

Figure 29: Comparisons with the existing methods on database: (a) UBIRIS.v2, (b) FRGC, (b) CASIA.v4-distance.
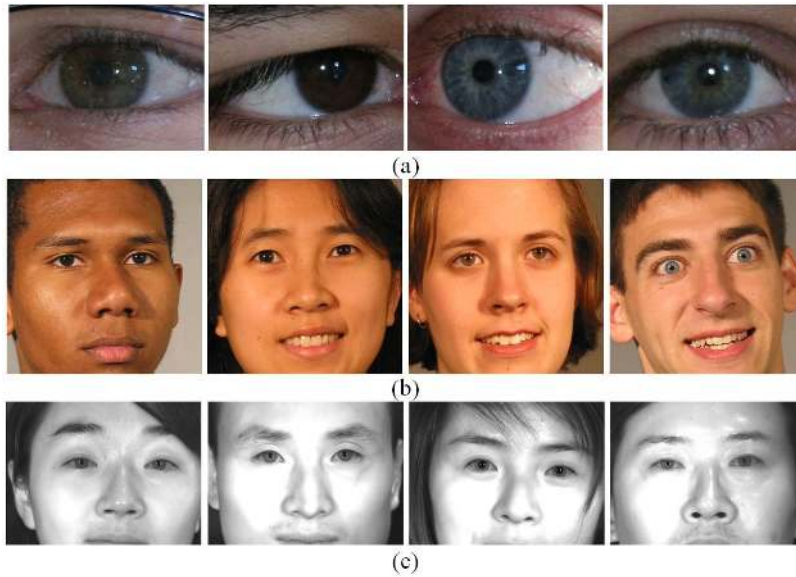

Figure 30: Sample images from (a) UBIRIS.v2, (b) FRGC (automatically cropped face), and (c) CASIA.v4-distance databases.

4. Conclusion

This paper has presented a promising approach for automated human recognition by simultaneously exploiting iris and periocular features to provide improved recognition performance. The developed iris segmentation approach is computationally attractive (Table 3) than previously proposed approaches especially for *visible illumination databases*. However, further efforts are still required to improve the efficiency of the iris segmentation algorithm in order to make it feasible for any possible online deployment in applications like remote surveillance. The experimental results obtained from the three publicly available at-a-distance databases, *i.e.*, UBIRIS.v2, FRGC and CASIA.v4-distance, clearly demonstrate the superior performance of the proposed segmentation technique, which suggest the

27

average improvement of 9.5%, 4.3% and 25.7% in segmentation accuracy respectively for the three employed databases. The developed segmentation approach not only achieves better segmentation accuracy but also with significantly reduced of computational cost and complexity as compared to the previous approaches. In order to improve the recognition accuracy, this paper exploits the joint strategy using the iris and periocular features. Rigorous experiments were carried out to evaluate the performance of various periocular feature extraction methods on the three employed databases. The best learned joint features from the experiments are also compared with the existing state-of-art algorithms, evaluated using the three employed databases, which reported an overall improvement of 52.4% in rank-one recognition accuracy. It is worth noting that only the single eye (left/right) images are employed in our work. The recognition accuracy is expected to be further improved if the information from both eyes can be simultaneously exploited. Such efforts for the performance improvement require new experiments and analysis which is to be pursued during our future work.

Acknowledgment

References

[1]   K. Bowyer, K. Hollingsworth, and P. Flynn, "Image understanding for iris biometrics: A survey," *Image & Vision Computing*, vol. 110, no. 2, pp. 281–307, 2008.

[2]   ISO/IEC 19794-6:2005. Information technology -- Biometric data interchange formats -- Part 6: Iris image data.

[3]   J. Daugman, "How iris recognition works," *IEEE Trans. Circuits Syst. Video Technol.*, vol. 14, no. 1, pp. 21–30, 2004.

[4]   H. Proenca and L. Alexandre, "UBIRIS: A noisy iris image database," *Proc. ICIAP 2005*, *Intern. Conf. Image Analysis and Processing*, vol. 1, 2005.

[5]   H. Proenca, S. Filipe, R. Santos, J. Oliveira, and L. Alexandre, "The UBIRIS.v2: A database of visible wavelength images captured on the move and at-a-distance," *IEEE Trans. Pattern Anal. Mach. Intell.*, vol. 32, no. 8, pp. 1529–1535, 2010.

[6]   H. Proenca, "Iris recognition: On the segmentation of degraded images acquired in the visible Wavelength," *IEEE Trans. Pattern Anal. Mach. Intell.*, vol. 32, no. 8, pp. 1502–1516, 2010.

[7]   T. Tan, Z. He, and Z. Sun, "Efficient and robust segmentation of noisy iris images for non-cooperative iris recognition," *Image Vision Comput.*, vol. 28, no. 2, pp. 223–230, 2010.

[8]   D. S. Jeong, J. W. Hwang, B. J. Kang, K. R. Park, C. S. Won, D.-K. Park and J. Kim, "A new iris segmentation method for non-ideal iris images," *Image Vision Comput.*, vol. 28, no. 2, pp. 254–260, 2010.

[9]   P. Li, X. Liu, L. Xiao and Q. Song, "Robust and accurate iris segmentation in very noisy iris images," *Image Vision Comput.*, vol. 28, no. 2, pp. 246–253, 2010.

[10]   W. Sankowski, K. Grabowski, M. Napieralska, M. Zubert and A. Napieralski, "Reliable algorithm for iris segmentation in eye image," *Image Vision Comput.*, vol. 28, no. 2, pp. 231–237, 2010.

[11] R. DonidaLabati and F. Scotti, "Noisy iris segmentation with boundary regularization and reflections removal," *Image Vision Comput.*, vol. 28, no. 2, pp. 270–277, 2010.

[12] Y. Chen, M. Adjouadi, C. Han, J. Wang, A. Barreto, N. Rishe and J. Andrian, "A highly accurate and computationally efficient approach for unconstrained iris segmentation," *Image Vision Comput.*, vol. 28, no. 2, pp. 261–269, 2010.

[13] M. A. Luengo-Oroz, E. Faure and J. Angulo, "Robust iris segmentation on uncalibrated noisy images using mathematical morphology," *Image Vision Comput.*, vol. 28, no. 2, pp. 278–284, 2010.

[14] Chun-Wei Tan and Ajay Kumar, "A unified framework for automated iris segmentation using distantly acquired face images," *IEEE Trans. Image Process.*, vol.21, no.9, pp.4068-4079, 2012.

[15] C.-W. Tan and A. Kumar, "Automated segmentation of iris images using visible wavelength face images," *Proc. CVPR 2011*, pp. 9–14, Colorado Springs, CVPRW'11, 2011.

[16] NICE.I - Noisy Iris Challenge Evaluation, Part I. http://nice1.di.ubi.pt/index.html.

[17] NICE:II - Noisy Iris Challenge Evaluation, Part II. http://nice2.di.ubi.pt/.

[18] Z. He, T. Tan, Z. Sun, and X. Qiu, "Toward accurate and fast iris segmentation for iris biometrics," *IEEE Trans. Pattern Anal. Mach. Intell.*, vol. 31, no. 9, pp. 1670–1684, 2009.

[19] A. Kumar and A. Passi, "Comparison and combination of iris matchers for reliable personal authentication," *Pattern Recognit.*, vol. 43, no. 3, pp. 1016–1026, 2010.

[20] J. Daugman, "New methods in iris recognition," *IEEE Trans. Syst. Man Cybern. Part B Cybern.*,vol. 37, no. 5, pp. 1167–1175, 2007.

[21] K. Miyazawa, K. Ito, T. Aoki, K. Kobayashi, and H. Nakajima, "An effective approach for iris recognition using phase-based image matching," *IEEE Trans. Pattern Anal. Mach. Intell.*, vol. 30, pp. 1741–1756, 2008.

[22] L. Masek and P. Kovesi, *MATLAB Source Code for a Biometric Identification System Based on Iris Patterns*, The School of Computer Science and Software Engineering, The University of Western Australia. 2003. http://www.csse.uwa.edu.au/~pk/studentprojects/libor/index.html.

[23] J.R. Matey, O. Naroditsky, K. Hanna, R. Kolczynski, D.J. LoIacono, S. Mangru, M. Tinker, T.M. Zappia, W.Y. Zhao, "Iris on the Move: Acquisition of Images for Iris Recognition in Less Constrained Environments," *Proc. of the IEEE*, vol.94, no.11, pp.1936-1947, 2006.

[24] S. Venugopalan, U. Prasad, K. Harun, K. Neblett, D. Toomey, J. Heyman, and M. Savvides, "Long Range Iris Acquisition System for Stationary and Mobile Subjects," *Proc. IJCB 2011*, pp.1–8, 2011.

[25] N. Kourkoumelis and M. Tzaphlidou, "Medical safety issues concerning the use of incoherent infrared light in biometrics," *in Ethics and Policy of Biometrics (A. Kumar and D. Zhang, Eds.)*, vol. 6005 of LNCS, pp. 121–126, Springer Berlin / Heidelberg, 2010.

[26] Am. Nat'l Standards Inst. "American National Standard for the Safe Use of Lasers and LEDs Used in Optical Fiber Transmission Systems," ANSI Z136.2, 1988.

[27] Commission Int'l de l'Eclarirage, "Photobiological Safety Standards for Safety Standards for Lamps," Report of TC 6-38; CIE 134-3-99, 1999.

[28] D. H. Brainard and B. A. Wandell, "Analysis of the retinex theory of color vision," *J. Opt. Soc. Am. A:*, vol.3, no. 10, pp.1651–1661, 1986.

[29] V. Štruc and N. Pavešić, "Performance Evaluation of Photometric Normalization Techniques for Illumination Invariant Face Recognition," *in Advances in Face Image Analysis: Techniques and Technologies*, Y.J. Zhang (*Ed.*), IGI Global.

[30] V. Štruc and N. Pavešić, "Gabor-Based Kernel Partial-Least-Squares Discrimination Features for Face Recognition," *Informatica (Vilnius)*, vol. 20, no. 1, pp.115–138, 2009.

[31] L. Grady, "Random Walks for Image Segmentation," *IEEE Trans. Pattern Anal. Mach. Intell.*, vol.28, no.11, pp. 1768–1783, 2006.

[32] J.A. Bondy and U.S.R. Murty, *Graph Theory*. Springer, 2008.

[33] M. Sonka, V. Hlavac and R. Boyle, *Image Processing, Analysis & and Machine Vision*, Thomson, pp. 144–146, 2008.

[34] G. Bradski, "The OpenCV Library," Dr. Dobb's Journal of Software Tools, 2000.

[35] P. Viola and M. Jones, "Rapid object detection using a boosted cascade of simple features," *Proc. CVPR 2001*, no., pp. 511–518, 2001.

[36] Face Recognition Grand Challenge – Overview. http://www.frvt.org/FRGC/.

[37] P. Phillips, P. Flynn, T. Scruggs, K. Bowyer, J. Chang, K. Hoffman, J. Marques, J. Min, and W.Worek, "Overview of the face recognition grand challenge," *Proc. 2005,* 2005.

[38] Biometrics Ideal Test. http://biometrics.idealtest.org/dbDetailForUser.do?id=4.

[39] Ground truth masks for iris segmentation.
http://www.comp.polyu.edu.hk/~csajaykr/myhome/research/GT.zip.

[40] D. Comaniciu and P. Meer, "Mean shift: A robust approach toward feature space analysis *IEEE Trans. Pattern Anal. Mach. Intell.*, vol. 24, pp. 603–619, 2002.

[41] V. Vezhnevets and V. Konouchine, "Grow-Cut - Interactive Multi-Label N-D Image Segmentation," *Proc. Graphicon*, pp. 150–156, 2005.

[42] D. L. Woodard, S. Pundlik, P. Miller, R. Jillela, and A. Ross, "On the Fusion of Periocular and Iris Biometrics in Non-ideal Imagery," *Proc. Intl. Conf. Pattern Recognition*, ICPR 2010, Istanbul (Turkey), pp.201-204, 2010.

[43] S. Bharadwaj, H.S. Bhatt, M. Vatsa, and R. Singh, "Periocular biometrics: When iris recognition fails," *Proc. BTAS 2010*, pp.1–6, 2010.

[44] U. Park, R. R. Jillela, A. Ross, and A. K. Jain, "Periocular biometrics in the visible spectrum," *IEEE Trans. Info. Forensics & Security*,vol. 6, no. 1, pp. 96–106, 2011.

[45] R.M da Costa and A. Gonzaga, "Dynamic Features for Iris Recognition," *IEEE Trans. Syst. Man Cybern. Part B Cybern.*, vol. X, no. X, pp.1–11, 2012. (*available online*)

[46] V. P. Pauca, M. Forkin, X. Xu, R. Plemmons and A. Ross, "Challenging Ocular Image Recognition," *Proc. of SPIE (Biometric Technology for Human Identification VIII)*, vol. 8029 80291V-1 – 80291V-13,2011.

[47] A. Oliva and A. Torralba, "Modeling the Shape of the Scene: A Holistic Representation of the Spatial Envelope," *International Journal of Computer Vision*, vol. 42, no. 3, pp. 145–175, 2001.

[48] T. Leung and J. Malik, "Representing and recognizing the visual appearance of materials using three-dimensional textons," *International Journal of Computer Vision*, vol. 43, no. 1, pp. 29–44, 2001.

[49] D. G. Lowe, "Distinctive image features from scale-invariant keypoints," *International Journal of Computer Vision*,vol. 60, no. 2, pp. 91–110, 2004.

[50] VLFeat: An Open and Portable Library of Computer Vision Algorithms. http://www.vlfeat.org/.

[51] A. Kumar, T.-S. Chan, "Iris recognition using quaternionic sparse orientation code (QSOC)," *Proc. CVPR 2012*, pp. 59-64, CVPRW 2012, Providence, June 2012.

[52] T. Ojala, M. Pietikainen and T. Maenpaa, "Multiresolution gray-scale and rotation invariant texture classification with local binary patterns," *IEEE Trans. Pattern Anal. Mach. Intell.*, vol. 24, no. 7, pp. 971–987, 2002.

[53] N. Dalal, B. Triggs, "Histograms of oriented gradients for human detection," *Proc. CVPR 2005*, pp.886–893, 2005.

[54] P. Armitage, G.Berry, and J. N. S. Matthews, *Statistical Methods in Medical Research* (4th edition). Blackwell Publishing, 2002.